

# Atomically Doped 2D Black Phosphorus for Efficient and Stable Perovskite Solar Cells

Abdulaziz S. R. Bati,\* Purevlkham Myagmarsereejid, Marco Fronzi, Kaicai Fan, Porun Liu, Yu Lin Zhong, Paul L. Burn, Ian R. Gentle, Paul E. Shaw, and Munkhbayar Batmunkh\*

Controlled functionalization of 2D black phosphorus (BP) nanosheets provides unique opportunities to tune their chemical, physical, and electronic properties. Herein, the preparation of single-atom nickel-doped BP (Ni-BP) sheets using a simple solution-based strategy is reported. Using the Ni-BP sheets as a passivation layer on top of a perovskite film leads to standard perovskite solar cells (PSCs) with improved performance. The standard *n-i-p* PSCs with the Ni-BP interlayer achieve maximum power conversion efficiencies of over 22%, with negligible hysteresis and a modest improvement in stability when subjected to different testing conditions. The perovskite films prepared with Ni-BP sheets-based passivation are found to have reduced defect densities as well as improved charge-transfer properties and carrier lifetimes. Density-functional theory calculations support the experimental results through showing that the atomic Ni-doping increases the work function of the BP interlayer, enabling better hole extraction, as well as increasing the surface hydrophobicity of the BP layer, hence reducing water sorption into the perovskite film.

single- and/or few-layered nanosheets obtained from bulk black phosphorus (BP) crystal were introduced as a new member of the family of 2D materials.<sup>[5]</sup> Since then, researchers have made excellent progress in BP research and showed that BP nanosheets exhibit unique defined and controllable electronic properties, including tunable bandgap, and high carrier mobility, making them attractive for optoelectronic and photovoltaic (PV) devices.<sup>[6–9]</sup>

Recently, research into exploring functionalization strategies and scaling up BP nanosheets has been the subject of intense investigations. The tunability of the properties of functionalized BP nanosheets and their application has gained increasing attention in materials research.<sup>[10]</sup> In this context, atomic doping using single-atoms (single-atom doping) as a means to precisely control the surface functionalization and properties of the materials has become an active research topic for BP sheets as well as other 2D materials.<sup>[11,12]</sup> Several theoretical studies have reported that single-atom doping of BP nanosheets should lead to modulation of their electronic structures and enhance their stability.<sup>[13,14]</sup> Despite the direction provided by the


## 1. Introduction

Two dimensional (2D)-layered materials such as graphene, transition-metal dichalcogenides, transition-metal carbides and nitrides (MXenes), and elemental 2D structures have been studied extensively over the past two decades.<sup>[1–4]</sup> About a decade ago,

precisely control the surface functionalization and properties of the materials has become an active research topic for BP sheets as well as other 2D materials.<sup>[11,12]</sup> Several theoretical studies have reported that single-atom doping of BP nanosheets should lead to modulation of their electronic structures and enhance their stability.<sup>[13,14]</sup> Despite the direction provided by the

A. S. R. Bati, P. L. Burn, I. R. Gentle, P. E. Shaw  
Centre for Organic Photonics & Electronics  
School of Chemistry and Molecular Biosciences  
The University of Queensland  
St Lucia, Brisbane, Queensland 4072, Australia  
E-mail: a.bati@uq.net.au

P. Myagmarsereejid, Y. L. Zhong, M. Batmunkh  
Queensland Micro- and Nanotechnology Centre  
School of Environment and Science  
Griffith University  
Nathan, Brisbane, Queensland 4111, Australia  
E-mail: m.batmunkh@griffith.edu.au

 The ORCID identification number(s) for the author(s) of this article can be found under <https://doi.org/10.1002/ssstr.202300334>.

© 2023 The Authors. Small Structures published by Wiley-VCH GmbH. This is an open access article under the terms of the Creative Commons Attribution License, which permits use, distribution and reproduction in any medium, provided the original work is properly cited.

DOI: 10.1002/ssstr.202300334

M. Fronzi  
School of Mathematical and Physical Science  
University of Technology Sydney  
Ultimo, New South Wales 2007, Australia

M. Fronzi  
School of Chemical and Biomedical Engineering  
University of Melbourne  
Parkville, VIC 3010, Australia

K. Fan, P. Liu  
Centre for Catalysis and Clean Energy  
Griffith University  
Southport, Gold Coast, Queensland 4222, Australia

K. Fan  
College of Materials Science and Engineering  
Qingdao University of Science and Technology  
Qingdao 266042, China

theoretical results and the use of atomic doping of 2D BP nanosheets in catalysis, these materials have not been studied to any extent in the context of solar cells. Examples of atomic doping of 2D BP nanosheets for catalysis include that of Wang et al.<sup>[15]</sup> who demonstrated excellent photocatalytic performance of lanthanum single-atom-doped BP, while Chen et al.<sup>[16]</sup> showed that BP nanosheets with palladium single-atom doping can act as efficient catalysts for organic transformations. Therefore, the development of simple strategies that can be used to effectively functionalize BP nanosheets at the atomic level would be of great value. It should be noted that single-atom doping of most 2D materials relies strongly on a high-temperature annealing step (>500 °C),<sup>[17]</sup> but the low sublimation temperature of BP (350–500 °C) makes the doping process very challenging.<sup>[18]</sup>

Single-junction organic–inorganic metal–halide perovskite solar cells (PSCs) have seen sustained attention owing to their distinctive optoelectronic properties, simple solution processability, and low fabrication costs. PSCs with a standard device architecture have now reached an exceptional certified power conversion efficiency (PCE) of over 26%, which makes them an appealing candidate for next-generation thin-film PV technologies.<sup>[19]</sup> Despite the enormous progress toward improving device efficiency, PSCs still suffer from poor long-term stability, limiting their widespread deployment and commercialization. Indeed, the intrinsic instability of the perovskite materials used in solar cells and their high sensitivity to moisture, heat, and short wavelength illumination are currently the key obstacles to realization of stable commercial devices.<sup>[20–22]</sup> Over the past few years, the operational stability of PSCs has been improved by composition tuning, additive incorporation, phase stabilization and surface passivation.<sup>[3,23–25]</sup> The latter method has been widely adopted as an effective approach to suppress the impact of surface defects of perovskite films, leading to improved charge extraction and hence device performance as well as stability. For example, it has been reported that small amounts of residual lead (II) iodide (PbI<sub>2</sub>) on the surface of the perovskite film can passivate the surface defects leading to improved efficiency and stability.<sup>[26]</sup> Recently, Ren et al.<sup>[27]</sup> introduced 3-(phenyl)propylammonium iodide (PPAI) as a perovskite-film surface treatment to inhibit iodide migration, which has been identified as a key issue that causes the rapid degradation of PSCs. The PPAI-treated n–i–p PSCs with a standard architecture showed excellent efficiency and improved stability, delivering a high

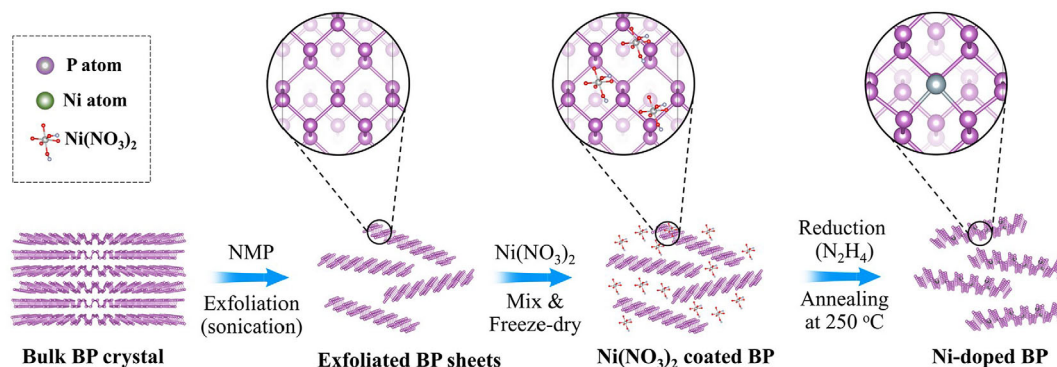
PCE of 24.2% and maintaining about 92% of their initial efficiency after being exposed to continuous light illumination at the maximum power point (MPP) under ambient conditions (relative humidity [RH] = 40 ± 5%). As such, the search for new functional materials that can be used as an efficient passivation layer for perovskite films is an active area of research.<sup>[28,29]</sup>

In this work, we report the synthesis of single-atom nickel-doped BP (Ni–BP) using a facile three-step solution-processing method (Figure 1). Considering their suitable energy band alignment and hydrophobic surface properties, the newly designed Ni–BP flakes were employed as an effective passivation layer on CsMAFAPbI<sub>3</sub>-based perovskite films for PSCs. A combination of experimental investigations and density-functional theory (DFT) calculations revealed that the use of the Ni–BP passivation layer reduced the defect density of the perovskite films, increased the charge-carrier lifetime and enhanced the overall device performance. More importantly, unencapsulated defect-passivated PSCs showed improved stability due to the enhanced surface hydrophobicity of the Ni–BP.

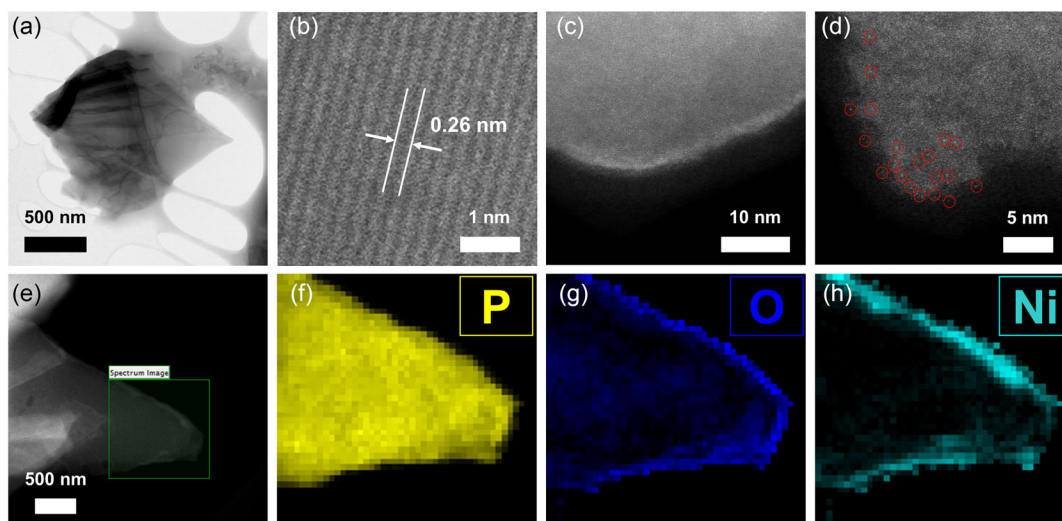
## 2. Results and Discussion

Figure 1 shows a schematic of the step-by-step synthesis procedure of the 2D Ni–BP nanosheets. In brief, bulk BP was exfoliated in *N*-methyl-2-pyrrolidone, followed by stirring with nickel(II) nitrate hexahydrate [Ni(NO<sub>3</sub>)<sub>2</sub>·6H<sub>2</sub>O] overnight. The weight ratio of BP and Ni(NO<sub>3</sub>)<sub>2</sub>·6H<sub>2</sub>O was 20:1. After centrifuging the solution, the precipitate containing BP and Ni(NO<sub>3</sub>)<sub>2</sub> was freeze-dried before being treated with hydrazine monohydrate vapor. Then, the sample was annealed at 250 °C under a flow of argon (Ar) to give the Ni–BP flakes.

To investigate the structural and chemical properties of the Ni–BP, transmission electron microscopy (TEM), high-resolution TEM (HRTEM), and energy-dispersive X-ray (EDX) spectroscopy elemental mapping images were collected. The TEM image shown in Figure 2a reveals that the Ni–BP flakes contain several 2D sheets with a relatively large lateral size (>500 nm). The lattice spacing of the Ni–BP was measured to be ≈0.26 nm (Figure 2b), demonstrating that the atomic Ni-doping did not distort the structural lattice of the BP.<sup>[30]</sup> It can be clearly observed from the HRTEM (Figure 2c) that the edge of the BP flakes was brighter after Ni-doping, indicating that the larger proportion of the doping has taken place on the BP



**Figure 1.** Schematic illustrating the nickel-doped black phosphorus (Ni–BP) preparation process.



**Figure 2.** a) Transmission electron microscopy (TEM) and b–d) high-resolution TEM images of the Ni–BP flakes. e–h) TEM electron-energy-loss spectroscopy elemental imaging of the Ni–BP flakes.

flake edges. However, Figure 2d shows that there are also single bright dots across the Ni–BP flake, which suggested that there was also Ni deposited across the surface of the BP flake. To determine whether this was the case, the presence of the different elements in the sample was investigated using electron-energy-loss spectroscopy (EELS) and EDX spectroscopy. The EELS and EDX elemental mapping images (Figure 2e–h; and Figure S1, Supporting Information) clearly show the existence of P, O, and Ni in the scanned area of the flake. The relatively strong Ni signal at the edge confirmed that single-atom Ni-doping occurred more effectively on the edge of BP flakes (Figure 2h) with significantly less (if any) on the surface of the flakes. This concentration of the Ni atoms on the edges of the BP sheet is consistent with theoretical and experimental studies showing that the edge sites are more reactive. For example, oxidation of 2D materials, including BP, often starts to occur at the edge.<sup>[31–33]</sup> Interestingly, the oxidized edges can also act as reactive sites to enhance their interaction with a dopant.<sup>[34]</sup>

Further evidence for the successful doping by atomic Ni of the BP flakes was confirmed using X-ray photoelectron spectroscopy (XPS) measurements, as illustrated in Figure 3a–c. The XPS survey scan, as shown in Figure 3a, displays the presence of P, O, and Ni, again demonstrating the successful preparation of Ni–BP. The relatively weak Ni signal in the XPS survey scan suggests that the amount of Ni in the sample is small, as expected based on the sample preparation method. High-resolution (HR) XPS spectra were used to explore the oxidation and doping states of the BP flakes. As shown in Figure 3b, the Ni–BP sample shows small peaks centered at a binding energy of around 129.5 eV. This peak can be deconvoluted into two main doublets with a splitting of 0.84 eV, which correspond to the P  $2p_{3/2}$  and P  $2p_{1/2}$  doublet associated with the P–P bonding.<sup>[35]</sup> Moreover, a broad peak at higher binding energies between 131.5 and 136.5 eV (centered at around 134.0 eV) can be observed for the Ni–BP sample. This broad peak is associated with the oxidized P ( $\text{PO}_x$ ).<sup>[34]</sup> Figure 3c displays the HR XPS of the Ni

$2p$  spectrum of the Ni–BP sample, which can be deconvoluted into three spin–orbit split doublets with a splitting of 17.5 eV. The binding energies of the Ni  $2p_{3/2}$  core level were located at 853.3, 856.1, and 860.7 eV, which can be ascribed to Ni, Ni– $\text{PO}_x$ , and the corresponding satellite peak, respectively.<sup>[36]</sup>

To further investigate the structural features of the Ni–BP flakes, X-ray-absorption spectroscopy (XAS) measurements were carried out. Figure 3d shows the Ni K-edge X-ray-absorption near-edge structure (XANES) spectra of the reference Ni foil, NiO, and Ni–BP samples. Unlike Ni foil ( $\text{Ni}^0$ ), the Ni–BP sample has an intense peak at a different onset energy, indicating a cationic coordination environment of the Ni sites. Interestingly, as displayed in Figure 3d, the Ni–BP sample had slightly lower valence energy than that of NiO ( $\text{Ni}^{2+}$ ), suggesting that the Ni center is coordinated mainly with the P atoms. This finding from the XANES spectra was consistent with the XPS results and previous literature on Ni–P interfaces.<sup>[37]</sup> The bonding environment was further studied using Fourier-transform extended X-ray-absorption fine structure (FT-EXAFS) spectroscopy (Figure 3e). The presence of a very low intensity peak at a high R-space (2.17 Å) indicates that the amount of metallic Ni ( $\text{Ni}^0$ ) in the Ni–BP sample was negligible. Furthermore, the local structures around the Ni sites of the Ni–BP sample were characteristic of Ni–P bonds, which exhibit slightly higher R-space values (1.67 Å) than the Ni–O bonds (1.62 Å) in the reference NiO sample. To gain further insight into the chemical configuration, EXAFS fitting was performed (Figure 3f), with the fitting parameters summarized in Table S1, Supporting Information (ESI). Notably, the Ni–P structure with a coordination number of six was used to fit the data. It can be clearly observed from Figure 3f that the measured (raw) data of the Ni–BP sample matches strongly with the fitted data of a Ni–P structure, indicating that the atomic Ni was mainly coordinated with the P atoms in the Ni–BP flakes.

To explore the effect of Ni–BP passivation on the perovskite films, XPS measurements were carried out on

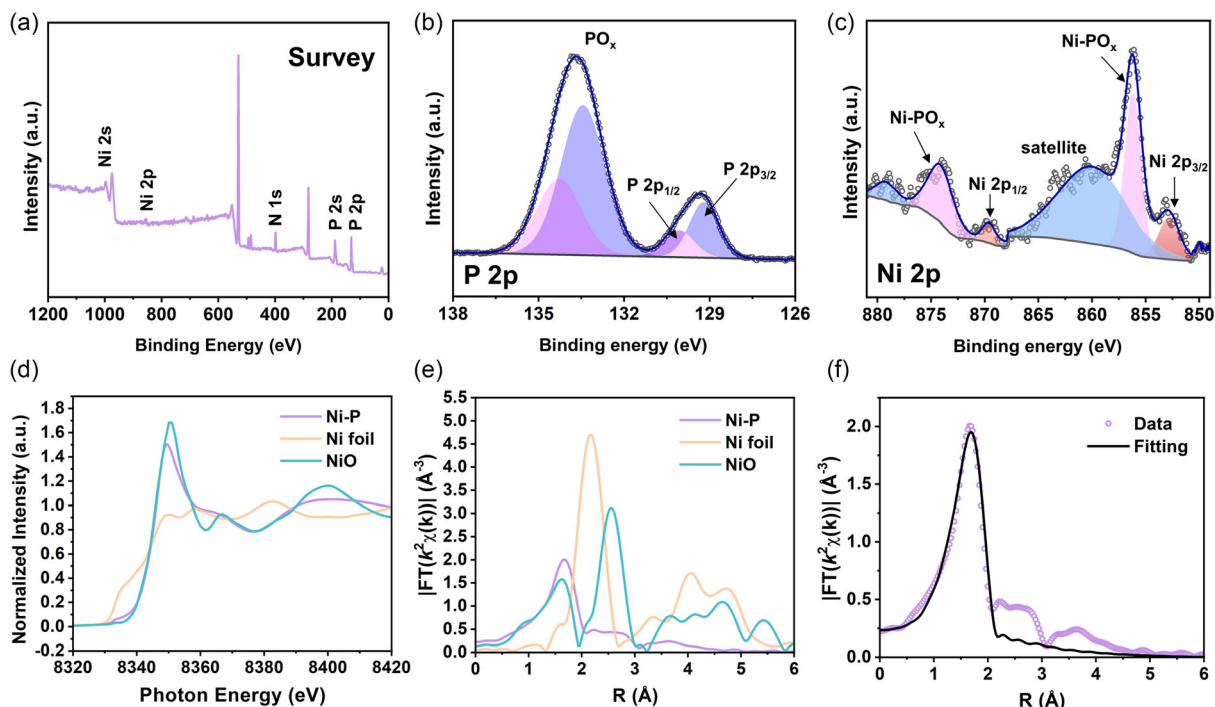


**Figure 3.** a) X-ray photoelectron spectroscopy (XPS) survey scan, b) high-resolution XPS (HR XPS) of the P  $2p$ , and c) HR XPS Ni  $2p$  spectra of the Ni-BP flakes. d) Normalized Ni K-edge X-ray-absorption near-edge structure spectra and e) Fourier transform–extended X-ray-absorption fine structure (FT-EXAFS) spectra of Ni foil, NiO, and Ni-BP samples. f) EXAFS raw data and fitting for the optimized model of the Ni-P structure.

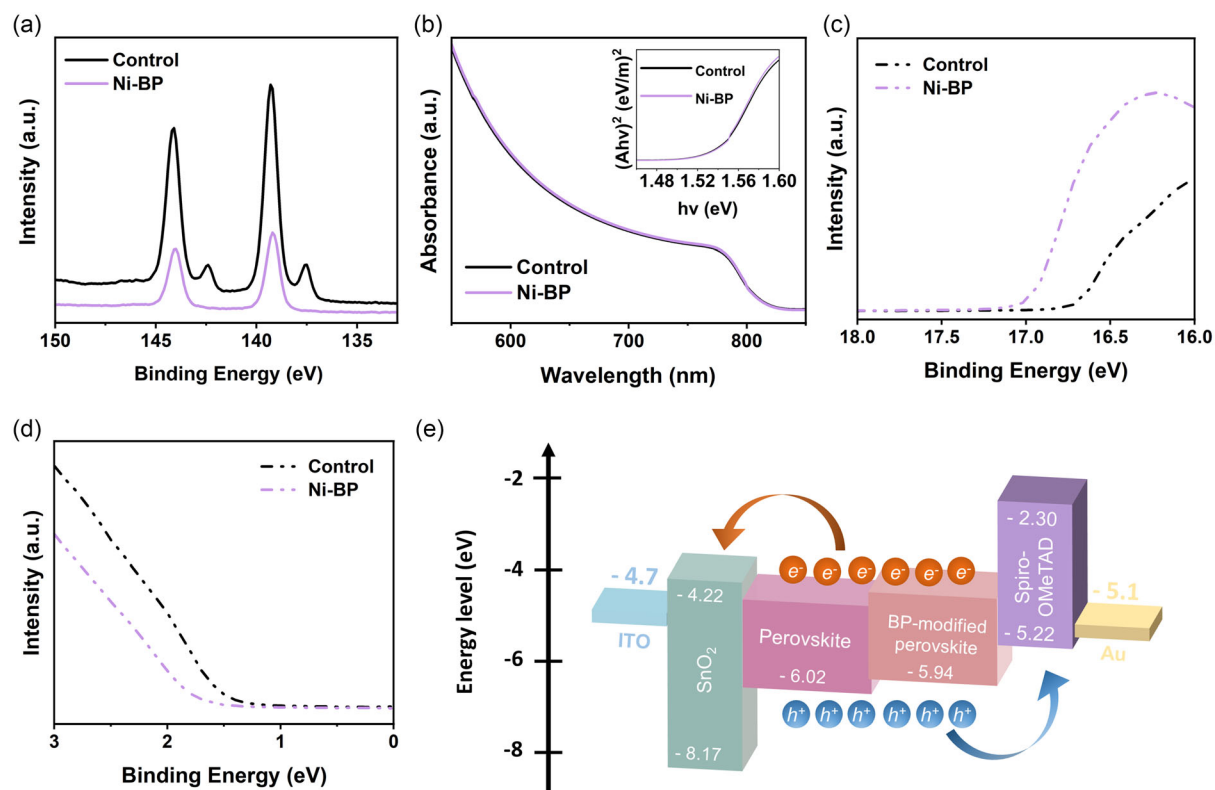


**Figure 4.** a) Pb  $4f$  core-level XPS spectra of perovskite films with and without (control) Ni-BP treatment. b) UV–vis spectra (inset shows Tauc plot). c) UPS spectra of the secondary electron cutoff and d) valence region of control and Ni-BP-treated perovskite films. e) Energy-level diagram showing each component of the PSCs.

$\text{Cs}_{0.01}\text{MA}_{0.01}\text{FA}_{0.98}\text{PbI}_3$  perovskite films with and without the surface treatment (Figure S2, Supporting Information). The Ni-BP was spin-coated onto the perovskite layer from a chlorobenzene solution, a solvent in which the perovskite was insoluble. It can be seen from the XPS Pb 4f core-level spectra (Figure 4a) that the neat control perovskite film had two additional peaks at 137.5 and 142.5 eV when compared to the perovskite film treated with Ni-BP flakes. The extra peaks in the untreated film correspond to spin-orbit split doublets with a splitting of 5.0 eV, which are assigned to metallic  $\text{Pb}^0$ . Thus, the untreated control film has iodide vacancies. After Ni-BP treatment, the  $\text{Pb}^0$  peaks disappeared, and a clear reduction in the intensity of the two main peaks corresponding to Pb 4f<sub>7/2</sub> and Pb 4f<sub>5/2</sub> was observed, indicating that the surface iodide vacancies have been removed.<sup>[25,38]</sup> Ultraviolet-visible (UV-vis)

absorption and ultraviolet photoelectron spectroscopy (UPS) spectra were conducted to further understand the effect of Ni-BP treatment on the perovskite films. As shown in Figure 4b, the Ni-BP treatment led to no significant changes in the UV-vis-absorption spectrum, which corresponds to the bulk light-absorption properties of the film. The bandgaps of the untreated control and Ni-BP-treated perovskite films were calculated to be around 1.55 eV. Analysis of the UPS data (Figure 4c,d) revealed that the valence band maximum was slightly less deep for the Ni-BP-passivated perovskite layer, which would be expected to lead to an improvement in charge extraction and an increase in the open-circuit voltage ( $V_{oc}$ ) of the devices (Figure 4e).

To evaluate the crystallinity of the perovskite film with and without the Ni-BP treatment, X-ray diffraction (XRD) analysis

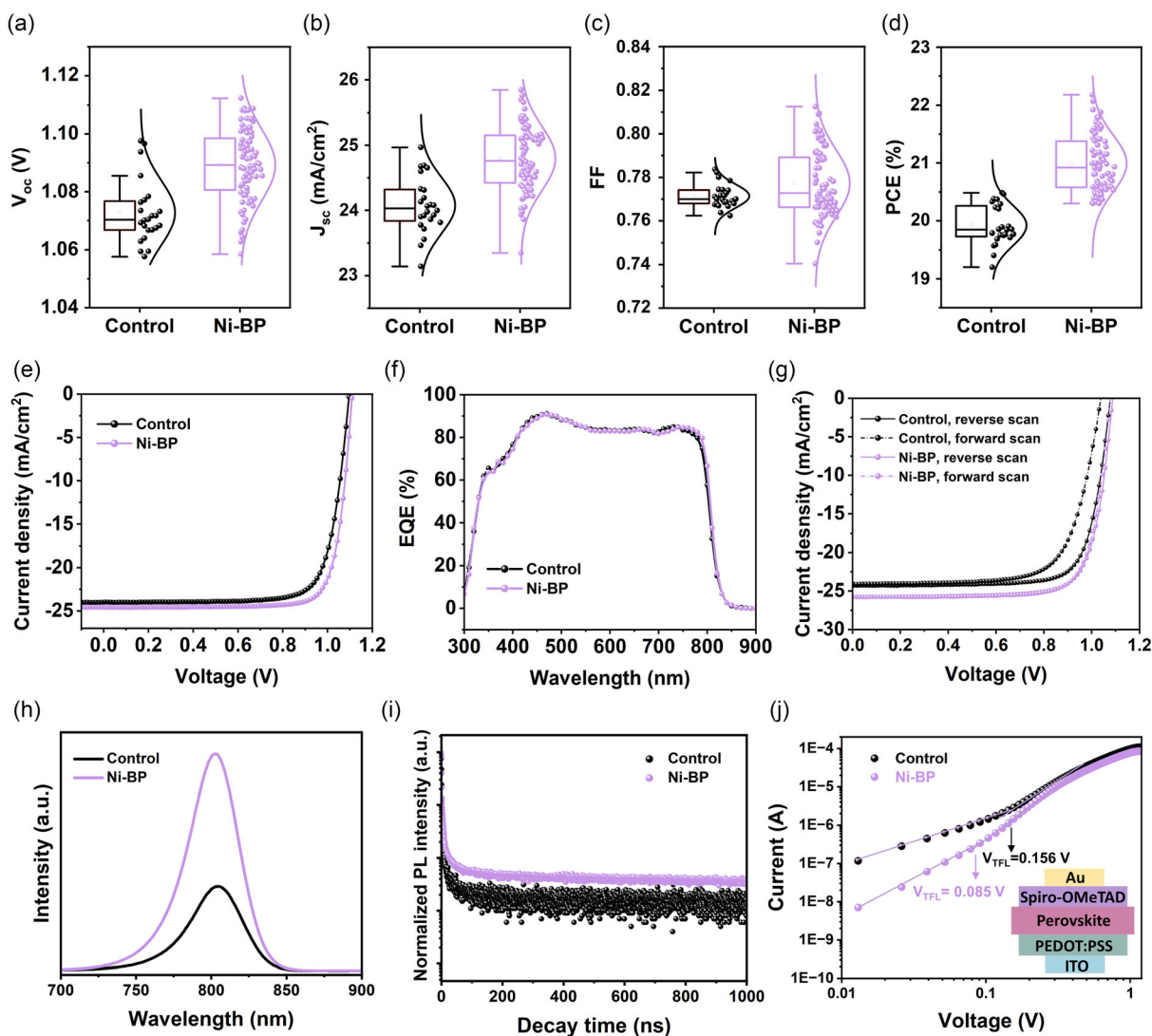


**Figure 5.** Statistical distribution of a) open-circuit voltage ( $V_{oc}$ ), b) short-circuit current density ( $J_{sc}$ ), c) fill factor (FF), and d) PCE of PSCs constructed with and without (control) Ni-BP passivation of the perovskite layer. e) Current density–voltage ( $J$ – $V$ ) curves and f) external quantum efficiency of the best-performing control and Ni-BP-treated devices. g)  $J$ – $V$  curves of the control and Ni-BP-treated devices measured in the forward and reverse scan directions. h) Photoluminescence (PL) spectra and i) time-resolved PL decays of perovskite films with and without (control) Ni-BP surface passivation on bare glass. j) Dark  $J$ – $V$  curves of the hole-only space-charge-limited-current devices.

was performed (Figure S3, Supporting Information). Compared to the perovskite film without Ni–BP treatment (the control film), the (001) diffraction peak of the residual  $\text{PbI}_2$  at  $12.6^\circ$  was weaker, indicating that the Ni–BP treatment reduced the  $\text{PbI}_2$  content. Controlling the amount of residual  $\text{PbI}_2$  is advantageous as excessive amounts can cause hysteresis in the current density–voltage ( $J$ – $V$ ) characteristics.<sup>[26]</sup> In comparison with the neat control film, the complete disappearance of the characteristic peak associated with the non-perovskite  $\delta$ -FAPbI<sub>3</sub> phase at  $11.7^\circ$  suggests that Ni–BP passivation stabilizes the active  $\alpha$ -FAPbI<sub>3</sub> phase by resisting moisture penetration and transformation to the  $\delta$ -FAPbI<sub>3</sub> phase.<sup>[39]</sup> Top-view scanning electron microscopy (SEM) images of the perovskite films with and without the Ni–BP surface treatment show that the two films have a similar surface morphology including average crystal grain sizes (Figure S4, Supporting Information).

To understand the effect of the Ni–BP treatment on the PV performance, PSCs with the configuration of indium-doped tin oxide (ITO)/ $\text{SnO}_2$ /perovskite/spiro-OMeTAD/Au with and without (control) the Ni–BP layer on top of the perovskite layer were fabricated and measured under standard 1 sun (AM 1.5G) solar illumination. Figure S4c, Supporting Information, displays the cross-sectional SEM of the complete device. The detailed PV parameters including  $V_{oc}$ , short-circuit current density ( $J_{sc}$ ), fill factor (FF), and PCE are summarized in Figure 5a–d. Figure 5e displays the  $J$ – $V$  characteristics of the champion devices with an active area of  $0.2\text{ cm}^2$ . As shown in Figure 5e, the best control devices without passivation delivered a maximum PCE of 20.5% with a  $V_{oc}$  of 1.10 V, a  $J_{sc}$  of  $24.0\text{ mA cm}^{-2}$ , and FF of 0.78. In contrast, the best Ni–BP-treated devices exhibited a significantly improved maximum PCE of 22.2% with a  $V_{oc}$  of 1.11 V, a  $J_{sc}$  of  $24.7\text{ mA cm}^{-2}$ , and a notable FF of 0.81. The PCE enhancement was derived from all the key characteristics, that is, an improved  $V_{oc}$ ,  $J_{sc}$ , and FF. The external quantum efficiency (EQE) spectra of the devices with and without Ni–BP treatment are shown in Figure 5f. The integrated  $J_{sc}$  values from the EQE spectra were calculated to be 23.0, and  $23.3\text{ mA cm}^{-2}$  for the control and Ni–BP-treated devices, respectively, both of which are within the accepted variance of the measured  $J_{sc}$ . In addition, one of the important tests for PV devices PSCs is the hysteresis behavior observed in the  $J$ – $V$  curves during measurements. Interestingly, in addition to the enhanced PCE, the hysteresis behavior was largely reduced for the devices with the Ni–BP passivation (Figure 5g). To quantitatively evaluate the hysteresis behavior of the devices, the hysteresis index (HI) can be calculated from the following equation.<sup>[40]</sup>

$$HI = \frac{PCE_{\text{reverse}} - PCE_{\text{forward}}}{PCE_{\text{reverse}}} \quad (1)$$

The HI was found to be significantly reduced from 0.118 to a negligible value of 0.001 after passivating the perovskite films with the Ni–BP flakes, suggesting that Ni–BP treatment reduces the surface defects of the perovskite film and reduces the charge accumulation at the perovskite/hole transporting layer (HTL) interface, both of which have been found to cause severe hysteresis.<sup>[41]</sup>

Further, steady-state photoluminescence (PL) and time-resolved PL (TRPL) measurements were used to study the

charge-carrier dynamics of the perovskite films before and after Ni–BP passivation. As shown in Figure 5h, the PL intensity of the Ni–BP-treated film was considerably higher as compared to the control perovskite film, with only a slight blueshift (2 nm) in the PL peak position. This can be attributed to the effective passivation of the perovskite surface, resulting in the suppression of trap-induced non-radiative charge recombination.<sup>[42]</sup> The suppression of surface defects was further confirmed by the increased average carrier lifetime from 16.9 to 40.8 ns after Ni–BP passivation (Figure 5i). Detailed TRPL parameters of the control and Ni–BP-treated perovskite films have been summarized in Table S2, Supporting Information. To estimate the effect of the Ni–BP on the trap-state density, space-charge-limited-current measurements were undertaken. Figure 5j presents the dark  $J$ – $V$  curves of a hole-only device with the structure of ITO/poly(3,4-ethylenedioxythiophene):poly(styrene sulfonate)/perovskite/spiro-OMeTAD/Au with and without Ni–BP passivation of the perovskite layer. The trap density ( $n_{\text{trap}}$ ) can be estimated according to the following equation.<sup>[43]</sup>

$$n_{\text{trap}} = \frac{2\epsilon_0\epsilon_r V_{\text{TFL}}}{eL^2} \quad (2)$$

where  $\epsilon_0$  is the vacuum permittivity ( $8.854 \times 10^{-12}\text{ F m}^{-1}$ ),  $\epsilon_r$  is the relative dielectric constant (28.8),  $V_{\text{TFL}}$  is the onset voltage of trap-filled limit,  $e$  is the elementary charge of the electron ( $1.60 \times 10^{-19}\text{ C}$ ), and  $L$  is the thickness of the perovskite film. As expected, the Ni–BP-treated device had a lower trap density of  $4.82 \times 10^{14}\text{ cm}^{-3}$  in comparison with the control device ( $8.84 \times 10^{14}\text{ cm}^{-3}$ ). These results clearly demonstrate the excellent passivation effect of Ni–BP flakes and are consistent with the PL and TRPL results. The PV parameters of our best-performing

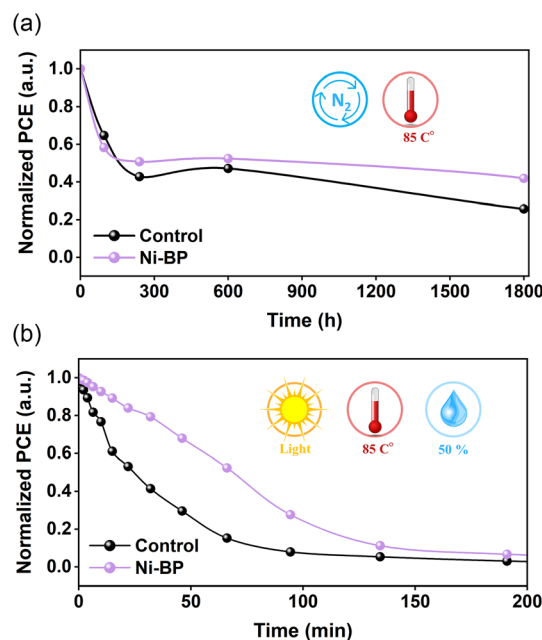


**Figure 6.** Stability tests of unencapsulated PSCs with and without (control) Ni–BP surface treatment aged a) at  $85^\circ\text{C}$  in a nitrogen atmosphere for 1800 h and b) at the maximum power point under continuous light irradiation at  $85^\circ\text{C}$  and 50% relative humidity for 200 h.

devices fabricated with Ni–BP passivation layer are compared with values reported in the literature for devices employing BP derivatives (Table S3, Supporting Information).

Given the good performance of the Ni–BP-treated PSCs, we next tested their stability following the International Summit on Organic Photovoltaic Stability (ISOS) protocols, specifically ISOS-D-2I and ISOS-L-2.<sup>[44]</sup> In the first part, we studied storage stability in an inert (N<sub>2</sub>) environment at 85 °C (Figure 6a). While both the control and treated PSCs showed an initial rapid drop in the PCE, the Ni–BP-treated device exhibited slightly better stability over 1800 h, retaining more than 40% of its initial PV performance, while the control device decayed to ≈20% of the initial PCE. We postulate that the slight improvement observed arises from the Ni–BP reducing the Pb content at the interface with the spiro-OMeTAD HTL, as evidenced by our XPS results, and inhibiting iodide ion migration from the perovskite to the spiro-OMeTAD. Iodide migration into the HTL has been reported to have an adverse effect on the charge extraction efficiency, leading to lower device efficiency, stability, and increased hysteresis.<sup>[45,46]</sup>

Furthermore, we conducted a stability test of the unencapsulated devices at the MPP under continuous light illumination at 85 °C in a room that had an RH of 50%. As shown in Figure 6b,

the control device showed a more rapid efficiency loss than that of the Ni–BP-treated perovskite-film-based device. In particular, the efficiency of the control cell declined to almost 0% of its initial PCE after aging over ≈100 min, while the Ni–BP-treated device was able to maintain about 30% of its original efficiency over the same time frame and under the same testing conditions. The improved stability can be attributed partially to the suppression of the defects at the perovskite/HTL interface and a reduction of water penetration into the perovskite films.

To gain a degree of insight into the improvements in the PSC performance through using the Ni–BP layer, we undertook a series of DFT calculations. First, the electronic structures of the BP and Ni–BP were calculated using the norm-conserving Troullier–Martins pseudopotential as implemented in Spanish Initiative for Electronic Simulations with Thousands of Atoms.<sup>[47]</sup> We developed the Ni–BP structure by doping the phosphorene layer with Ni atoms (Figure 7a) and then compared it with a pure BP lattice. The partial density of states calculations for individual atoms are depicted in Figure 7b. According to the DFT calculations, the work function changed from –4.87 to –4.84 eV in moving from the pure phosphorene to the Ni–BP, which is consistent with the UPS measurements.

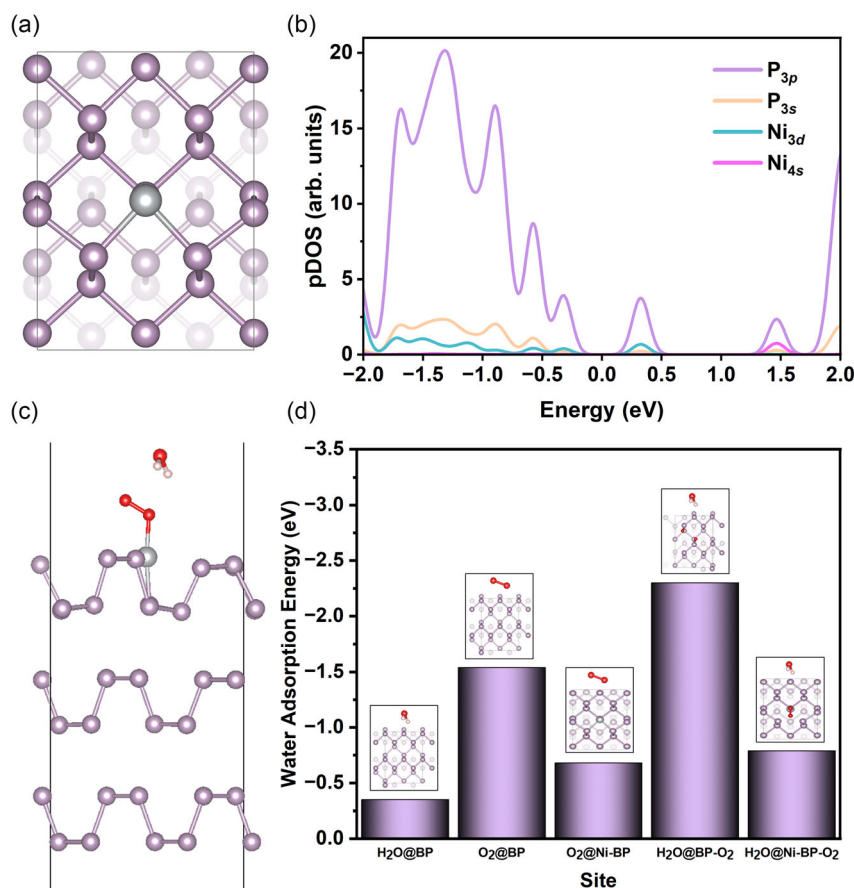


**Figure 7.** a) Optimized structure of Ni–BP and b) the corresponding partial density of states (PDOS) calculations for individual atoms. c) Adsorption of H<sub>2</sub>O on the Ni–BP structure after O<sub>2</sub> molecule adsorption. d) Calculated adsorption free energy of H<sub>2</sub>O and O<sub>2</sub> molecules on different surfaces. Although a pure BP surface shows good hydrophobicity, considering the practical challenges, O<sub>2</sub> molecules were adsorbed on the BP and Ni–BP surfaces before calculating the adsorption energies of H<sub>2</sub>O.

Moreover, we performed DFT calculations to evaluate the surface hydrophobicity by calculating the adsorption free energy of water on the different structures (Figure 7c,d). The surface hydrophobicity is particularly important for the device stability in humid conditions. As shown in Figure 7d, a pure BP surface is relatively hydrophobic in accordance with previous studies.<sup>[34,48]</sup> However, it is clear based on the adsorption energy values of oxygen (O<sub>2</sub>) and water (H<sub>2</sub>O) that the pure BP tends to adsorb O<sub>2</sub> molecules more rapidly than H<sub>2</sub>O. Thus, in calculating the adsorption energies of H<sub>2</sub>O on the surface, one needs to take into account that O<sub>2</sub> has been preadsorbed and has likely reacted to give PO<sub>x</sub> as shown earlier in the HR XPS measurements.<sup>[8]</sup> Therefore, we calculated the adsorption energies of H<sub>2</sub>O molecules after adsorbing O<sub>2</sub> molecules onto the pure BP and Ni-BP surfaces. It can be seen from Figure 7d that single-atom Ni doping can significantly increase the hydrophobicity of BP surface, demonstrating that the Ni-BP passivation layer can protect the perovskite layer from moisture ingress and subsequent degradation. To validate this theoretical finding, the water contact angles of the control and Ni-BP-treated perovskite films were measured (Figure S5, Supporting Information). The contact angle of the Ni-BP-treated film was measured to be 89°, which is considerably higher than that of the neat BP film (55°). This indicates a significantly enhanced film hydrophobicity, which is beneficial for moisture resistivity and hence improved device operational stability under humid conditions.

### 3. Conclusions

In conclusion, we have developed a novel and effective strategy for introducing single-atom Ni doping onto BP flakes composed of a small number of layers and demonstrated that high efficiency PSCs increased stability can be fabricated using Ni-BP as a surface passivation layer on the perovskite film. Through XAS and HRTEM measurements, we confirmed that the Ni was primarily anchored onto the edge of the BP flakes. The introduction of Ni doping increased the work function of the BP, and also increased the surface hydrophobicity, making the Ni-BP flakes highly suitable as a passivation layer for standard PSCs. By employing the Ni-BP passivation layer, not only were the optoelectronic properties of the perovskite films and devices enhanced, but the trap-state densities were reduced. As a result, the Ni-BP-treated devices showed significantly improved PCEs of over 22% with negligible hysteresis. Importantly, the unencapsulated Ni-BP-treated PSCs exhibited improved stabilities under the testing conditions of high temperature and humidity. Both the experimental measurements and DFT calculations confirmed that the surface hydrophobicity of Ni-BP plays a critical role in improving device stability. We believe that our strategy offers a new direction for the controllable doping of 2D materials, which can be used not only to fabricate highly efficient and more stable PSCs but also other optoelectronic devices. Thus, this work opens a new avenue for employing low-dimensional materials as effective surface treatments for PSCs. Future studies should focus on developing strategies that can be used to prepare uniformly doped BP sheets

with large lateral sizes to enable fabrication of large-area devices with improved stabilities.

### Supporting Information

Supporting Information is available from the Wiley Online Library or from the author.

### Acknowledgements

This work was financially supported by the Australian Research Council (grant no. DE220100521) and the Australian Government through the Australian Renewable Energy Agency (ARENA). The Australian Government, through ARENA, is supporting Australian research and development in solar PV and solar thermal technologies to help solar power become cost competitive with other energy sources. The views expressed herein are not necessarily the views of the Australian Government, and the Australian Government does not accept responsibility for any information or advice contained herein. A.S.R.B. acknowledges support from King Abdullah University of Science and Technology (KAUST) through the Ibn Rushd Postdoctoral Fellowship Award. The authors thank Dr. Ashley Slattery of Adelaide Microscopy at the University of Adelaide for his help with TEM analysis. The authors gratefully acknowledge the use of Centre for Microscopy and Microanalysis (CMM) facilities at the University of Queensland, Australia. This work was performed in part at the Queensland node of the Australian National Fabrication Facility. A company established under the National Collaborative Research Infrastructure Strategy provides nano- and microfabrication facilities for Australia's researchers. P.L.B. is a University of Queensland Laureate Fellow.

Open access publishing facilitated by Griffith University, as part of the Wiley - Griffith University agreement via the Council of Australian University Librarians.

### Conflict of Interest

The authors declare no conflict of interest.

### Data Availability Statement

The data that support the findings of this study are available from the corresponding author upon reasonable request.

### Keywords

2D materials, black phosphorus, perovskite solar cells, stabilities

Received: September 4, 2023  
Published online: October 17, 2023

- [1] M. Acik, S. B. Darling, *J. Mater. Chem. A* **2016**, *4*, 6185.
- [2] A. S. R. Bati, M. Batmunkh, J. G. Shapter, *Adv. Energy Mater.* **2020**, *10*, 1902253.
- [3] A. S. R. Bati, A. A. Sutanto, M. Hao, M. Batmunkh, Y. Yamauchi, L. Wang, Y. Wang, M. K. Nazeeruddin, J. G. Shapter, *Cell Rep. Phys. Sci.* **2021**, *2*, 100598.
- [4] S. Suragtkhuu, S. Sunderiya, P. Myagmarsereejid, S. Purevdorj, A. S. R. Bati, B. Bold, Y. L. Zhong, S. Davaasambu, M. Batmunkh, *Adv. Energy Mater.* **2023**, *13*, 2204074.



- [5] L. Li, Y. Yu, G. J. Ye, Q. Ge, X. Ou, H. Wu, D. Feng, X. H. Chen, Y. Zhang, *Nat. Nanotechnol.* **2014**, *9*, 372.
- [6] M. Batmunkh, M. Bat-Erdene, J. G. Shapter, *Adv. Energy Mater.* **2018**, *8*, 1701832.
- [7] A. Carvalho, M. Wang, X. Zhu, A. S. Rodin, H. Su, A. H. Castro Neto, *Nat. Rev. Mater.* **2016**, *1*, 16061.
- [8] M. Batmunkh, M. Bat-Erdene, J. G. Shapter, *Adv. Mater.* **2016**, *28*, 8586.
- [9] M. Zhang, G. M. Biesold, Z. Lin, *Chem. Soc. Rev.* **2021**, *50*, 13346.
- [10] X. Liu, L. Xiao, J. Weng, Q. Xu, W. Li, C. Zhao, J. Xu, Y. Zhao, *Sci. Adv.* **2020**, *6*, eabb4359.
- [11] H. Jiang, W. Yang, M. Xu, E. Wang, Y. Wei, W. Liu, X. Gu, L. Liu, Q. Chen, P. Zhai, X. Zou, P. M. Ajayan, W. Zhou, Y. Gong, *Nat. Commun.* **2022**, *13*, 6863.
- [12] B. Zhang, T. Fan, N. Xie, G. Nie, H. Zhang, *Adv. Sci.* **2019**, *6*, 1901787.
- [13] X. Zhao, Y. Pei, *J. Phys. Chem. C* **2021**, *125*, 12541.
- [14] P. Ou, X. Zhou, F. Meng, C. Chen, Y. Chen, J. Song, *Nanoscale* **2019**, *11*, 13600.
- [15] Q. Wang, L. Dong, M. Li, H. Lu, G. Wei, Y. Qu, G. Wang, *Adv. Funct. Mater.* **2022**, *32*, 2207330.
- [16] C. Chen, W. Ou, K.-M. Yam, S. Xi, X. Zhao, S. Chen, J. Li, P. Lyu, L. Ma, Y. Du, W. Yu, H. Fang, C. Yao, X. Hai, H. Xu, M. J. Koh, S. J. Pennycook, J. Lu, M. Lin, C. Su, C. Zhang, J. Lu, *Adv. Mater.* **2021**, *33*, 2008471.
- [17] S. Zhou, L. Shang, Y. Zhao, R. Shi, G. I. N. Waterhouse, Y.-C. Huang, L. Zheng, T. Zhang, *Adv. Mater.* **2019**, *31*, 1900509.
- [18] M. Fortin-Deschênes, P. L. Levesque, R. Martel, O. Moutanabbir, *J. Phys. Chem. Lett.* **2016**, *7*, 1667.
- [19] A. S. R. Bati, Y. L. Zhong, P. L. Burn, M. K. Nazeeruddin, P. E. Shaw, M. Batmunkh, *Commun. Mater.* **2023**, *4*, 2.
- [20] R. Prasanna, T. Leijtens, S. P. Dunfield, J. A. Raiford, E. J. Wolf, S. A. Swifter, J. Werner, G. E. Eperon, C. de Paula, A. F. Palmstrom, C. C. Boyd, M. F. A. M. van Hest, S. F. Bent, G. Teeter, J. J. Berry, M. D. McGehee, *Nat. Energy* **2019**, *4*, 939.
- [21] Y. Zhang, A. Kirs, F. Ambroz, C.-T. Lin, A. S. R. Bati, I. P. Parkin, J. G. Shapter, M. Batmunkh, T. J. Macdonald, *Small Methods* **2021**, *5*, 2000744.
- [22] A. S. R. Bati, M. Hao, T. J. Macdonald, M. Batmunkh, Y. Yamauchi, L. Wang, J. G. Shapter, *Small* **2021**, *17*, 2101925.
- [23] N. J. Jeon, J. H. Noh, W. S. Yang, Y. C. Kim, S. Ryu, J. Seo, S. I. Seok, *Nature* **2015**, *517*, 476.
- [24] Z. Qiu, N. Li, Z. Huang, Q. Chen, H. Zhou, *Small Methods* **2020**, *4*, 1900877.
- [25] Q. Jiang, Y. Zhao, X. Zhang, X. Yang, Y. Chen, Z. Chu, Q. Ye, X. Li, Z. Yin, J. You, *Nat. Photonics* **2019**, *13*, 460.
- [26] Q. Jiang, Z. Chu, P. Wang, X. Yang, H. Liu, Y. Wang, Z. Yin, J. Wu, X. Zhang, J. You, *Adv. Mater.* **2017**, *29*, 1703852.
- [27] G. Ren, Z. Zhang, Y. Deng, Z. Li, C. Liu, M. Wang, W. Guo, *Energy Environ. Sci.* **2023**, *16*, 565.
- [28] F. H. Isikgor, S. Zhumagali, L. V. T. Merino, M. De Bastiani, I. McCulloch, S. De Wolf, *Nat. Rev. Mater.* **2023**, *8*, 89.
- [29] G. Wu, R. Liang, M. Ge, G. Sun, Y. Zhang, G. Xing, *Adv. Mater.* **2022**, *34*, 2105635.
- [30] M. Zhu, X. Cai, M. Fujitsuka, J. Zhang, T. Majima, *Angew. Chem., Int. Ed.* **2017**, *56*, 2064.
- [31] K. L. Kuntz, R. A. Wells, J. Hu, T. Yang, B. Dong, H. Guo, A. H. Woomer, D. L. Druffel, A. Alabanza, D. Tománek, S. C. Warren, *ACS Appl. Mater. Interfaces.* **2017**, *9*, 9126.
- [32] X. Zhu, T. Zhang, D. Jiang, H. Duan, Z. Sun, M. Zhang, H. Jin, R. Guan, Y. Liu, M. Chen, H. Ji, P. Du, W. Yan, S. Wei, Y. Lu, S. Yang, *Nat. Commun.* **2018**, *9*, 4177.
- [33] S. KC, R. C. Longo, R. M. Wallace, K. Cho, *J. Appl. Phys.* **2015**, *117*, 135301.
- [34] G. Xu, H. Li, A. S. R. Bati, M. Bat-Erdene, M. J. Nine, D. Losic, Y. Chen, J. G. Shapter, M. Batmunkh, T. Ma, *J. Mater. Chem. A* **2020**, *8*, 15875.
- [35] R. Jain, Y. Singh, S.-Y. Cho, S. P. Sasikala, S. H. Koo, R. Narayan, H.-T. Jung, Y. Jung, S. O. Kim, *Chem. Mater.* **2019**, *31*, 2786.
- [36] F. Yu, H. Zhou, Y. Huang, J. Sun, F. Qin, J. Bao, W. A. Goddard, S. Chen, Z. Ren, *Nat. Commun.* **2018**, *9*, 2551.
- [37] P. F. Liu, X. Li, S. Yang, M. Y. Zu, P. Liu, B. Zhang, L. R. Zheng, H. Zhao, H. G. Yang, *ACS Energy Lett.* **2017**, *2*, 2257.
- [38] Y. Du, J. Wu, X. Zhang, Q. Zhu, M. Zhang, X. Liu, Y. Zou, S. Wang, W. Sun, *J. Energy Chem.* **2021**, *52*, 84.
- [39] X. Chen, Y. Xia, Z. Zheng, X. Xiao, C. Ling, M. Xia, Y. Hu, A. Mei, R. Cheacharoen, Y. Rong, H. Han, *Chem. Mater.* **2022**, *34*, 728.
- [40] Z. Li, J. Tinkham, P. Schulz, M. Yang, D. H. Kim, J. Berry, A. Sellinger, K. Zhu, *Adv. Energy Mater.* **2017**, *7*, 1601451.
- [41] D.-H. Kang, N.-G. Park, *Adv. Mater.* **2019**, *31*, 1805214.
- [42] H. Guo, Y. Fang, H.-B. Cheng, J. Wu, Y. Lei, S. Wang, X. Li, Y. Dai, W. Xiang, D.-J. Xue, Y. Lin, A. Hagfeldt, *Angew. Chem., Int. Ed.* **2022**, *61*, e202204148.
- [43] Y. Zhang, X. Liu, P. Li, Y. Duan, X. Hu, F. Li, Y. Song, *Nano Energy* **2019**, *56*, 733.
- [44] M. V. Khenkin, E. A. Katz, A. Abate, G. Bardizza, J. J. Berry, C. Brabec, F. Brunetti, V. Bulović, Q. Burlingame, A. Di Carlo, R. Cheacharoen, Y.-B. Cheng, A. Colmann, S. Cros, K. Domanski, M. Dusza, C. J. Fell, S. R. Forrest, Y. Galagan, D. Di Girolamo, M. Grätzel, A. Hagfeldt, E. von Hauff, H. Hoppe, J. Kettle, H. Köbler, M. S. Leite, S. Liu, Y.-L. Loo, J. M. Luther, et al., *Nat. Energy* **2020**, *5*, 35.
- [45] C. Li, S. Tscheuschner, F. Paulus, P. E. Hopkinson, J. Kießling, A. Köhler, Y. Vaynzof, S. Huettner, *Adv. Mater.* **2016**, *28*, 2446.
- [46] G. Tumen-Ulzii, C. Qin, T. Matsushima, M. R. Leyden, U. Balijipalli, D. Klotz, C. Adachi, *Sol. RRL* **2020**, *4*, 2000305.
- [47] M. S. José, A. Emilio, D. G. Julian, G. Alberto, J. Javier, O. Pablo, S.-P. Daniel, *J. Phys.: Condens. Matter* **2002**, *14*, 2745.
- [48] Y. Huang, J. Qiao, K. He, S. Bliznakov, E. Sutter, X. Chen, D. Luo, F. Meng, D. Su, J. Decker, W. Ji, R. S. Ruoff, P. Sutter, *Chem. Mater.* **2016**, *28*, 8330.